

Strain-driven diffusion process during silicon oxidation investigated by coupling density functional theory and activation relaxation technique

N. Salles, N. Richard, N. Mousseau, and A. Hemeryck

Citation: *The Journal of Chemical Physics* **147**, 054701 (2017); doi: 10.1063/1.4996206

View online: <http://dx.doi.org/10.1063/1.4996206>

View Table of Contents: <http://aip.scitation.org/toc/jcp/147/5>

Published by the [American Institute of Physics](#)



**COMPLETELY
REDESIGNED!**

**PHYSICS
TODAY**

Physics Today Buyer's Guide
Search with a purpose.

Strain-driven diffusion process during silicon oxidation investigated by coupling density functional theory and activation relaxation technique

N. Salles,¹ N. Richard,² N. Mousseau,³ and A. Hemeryck^{1,a)}

¹LAAS CNRS, Université de Toulouse, CNRS, Toulouse, France

²CEA, DAM, DIF, Bruyères-le-Châtel, F-91297 Arpajon, France

³Département de Physique, Université de Montréal, C.P. 6128, Succursale Centre-Ville, Montréal, Québec H3C 3J7, Canada

(Received 22 November 2016; accepted 14 July 2017; published online 1 August 2017)

The reaction of oxygen molecules on an oxidized silicon model-substrate is investigated using an efficient potential energy hypersurface exploration that provides a rich picture of the associated energy landscape, energy barriers, and insertion mechanisms. Oxygen molecules are brought in, one by one, onto an oxidized silicon substrate, and accurate pathways for sublayer oxidation are identified through the coupling of density functional theory to the activation relaxation technique nouveau, an open-ended unbiased reaction pathway searching method, allowing full exploration of potential energy surface. We show that strain energy increases with O coverage, driving the kinetics of diffusion at the Si/SiO₂ interface in the interfacial layer and deeper into the bulk: at low coverage, interface reconstruction dominates while at high coverage, oxygen diffusion at the interface or even deeper into the bottom layers is favored. A changing trend in energetics is observed that favors atomic diffusions to occur at high coverage while they appear to be unlikely at low coverage. Upon increasing coverage, strain is accumulated at the interface, allowing the oxygen atom to diffuse as the strain becomes large enough. The observed atomic diffusion at the interface releases the accumulated strain, which is consistent with a layer-by-layer oxidation growth. *Published by AIP Publishing.* [<http://dx.doi.org/10.1063/1.4996206>]

I. INTRODUCTION

For more than fifty years, silicon (Si) and its oxide, silica (SiO₂), have been the materials of choice in the field of microelectronics notably because of the remarkable quality of its interface in which SiO₂ serves as a gate oxide on the silicon substrate into Metal Oxide Semiconductor Field-Effect Transistors (MOSFETs).¹ More recently, this interface has also been used in Metal-Insulator-Semiconductor (MIS) nanojunctions² and in silicon spintronics³ among other applications. Moreover, in many applicative systems, the growth of a different oxide layer on a silicon substrate first requires the preparation of a thin silica layer between the silicon and the oxide. A total control of the growth, the thickness, and the quality of this layer is then mandatory in order to obtain the desired properties for the components as illustrated by the case of hafnia-based MOSFETs.⁴ From a more fundamental point of view, this interface is a model system for growing an oxide on a semiconductor but also for the formation of an amorphous from a crystalline system. Yet, despite intensive experimental (Refs. 5–12 and references therein) and theoretical studies,^{13–24} many fundamental questions about the basic mechanisms of the early formation stages of this crystalline/amorphous interface, including the role of strain-driven reactions, remain unresolved. Strain effect appears to

be at the origin of the emission of interstitial silicon atoms at the interface allowing the transition from a dense silicon substrate to an amorphous oxide.^{8,9,25,26} A layer-by-layer growth mode as observed in silicon thermal oxidation has also been attributed to a strain-driven propagation of the oxidation front.^{25–28} A relation between oxidation coverage, temperature dependency, and interfacial strain has been established.^{8,29,30} More recently, a retarded or self-limiting oxidation of silicon nanowires has been also attributed to mechanical effects.^{31–33} A comprehensive atomic-scale view of silica growth is still lacking.

To advance on this issue, we follow an innovative approach: starting from previously calculated configurations for the first oxidized layer, we use the Activation Relaxation Technique (ART nouveau or ARTn)^{34–36} coupled with first principles calculations using the VASP package.^{37,38} The choice of Density Functional Theory (DFT) based calculations allows us to describe precisely all the atomic and electronic structure variations associated with oxidation such as spin transition and charge transfer.

For up to a monolayer of oxide coverage, it is still possible to explore the configurational space by hand. However, as oxygen molecules are further added, the number of possible configurations and diffusion paths in the subsurface and deeper into the bulk, crucial to the growth of the oxidized layer, rapidly increases, involving complex mechanisms associated with large rearrangements and the displacement of several atoms. In such cases, double-ended methods to determine minimum energy pathways, such as the nudged elastic

^{a)} Author to whom correspondence should be addressed: anne.hemeryck@laas.fr

band method, are insufficient as they require a pre-knowledge or a guess of the final configuration. It is necessary to turn, rather, to open-ended search methods, such as the Activation Relaxation Technique nouveau (ARTn),^{34–36} Eigenvector Following (EF),³⁹ or the dimer method,⁴⁰ that allow the unbiased exploration of space configurations and diffusion mechanisms. For silicon oxidation, ARTn seems well fitted to the problems we address. As an open-ended saddle point search algorithm, this algorithm has already clearly demonstrated its efficiency to explore a set of configurations even in complex disordered systems and defect diffusion.^{41,42} Furthermore, it has already been used for a systematic study on silicon oxidation using empirical potentials showing its applicability to this issue by performing the diffusion and insertion of the oxygen atoms into the silicon-silicon bonds and supplying the energy barriers between the various generated configurations.⁴³

At the initial stage, Si(100) oxidation grows layer-by-layer,^{5,6} and the oxidation rate change is strongly correlated with the amount of strained Si at the interface.⁸ These experimental results suggest a Si oxidation model mediated by point defect generation (emitted Si atoms and their vacancies) due to the oxidation-induced strain.^{7–9} The aim of this article is to develop a detailed atomic-scale understanding of the propagation of the oxidation rate starting from a simple oxidized model system, with a particular focus on the correlation between the strain at the interface and the oxidation propagation rate, an aspect that is very difficult to characterize experimentally. To do so, we start from configurations observed in previous DFT studies^{8–10,16,17,43,44} on the first monolayer oxidation. Oxygen coverage is then increased, and oxygen adsorption and further diffusion at the Si/SiO₂ interface are studied using VASP-ARTn coupling. This approach allows us to establish a direct link between the subsurface diffusion mechanism in close relation with the strain energy and its effect on the energetics in terms of kinetics and energy gains.

II. METHODOLOGY

A. ART nouveau

The Activation Relaxation Technique nouveau (ARTn) method allows an efficient and unbiased search of possible migration paths for an atom in a given system. ARTn explores the potential energy surface (PES) and determines possible transition states, i.e., the different configurations and their corresponding activation barriers from a given starting configuration, without the need for prior knowledge of the final states.

ARTn proceeds in three steps: (1) From a local energy minimum, a random deformation is applied in order to leave the harmonic basin. As the system is slowly deformed, the structure is partially relaxed in a hyperplane orthogonal to this displacement and the lowest eigenvalue of the Hessian matrix is calculated with 10–15 force evaluations using the Lanczos algorithm. (2) Once a negative eigenvalue is found, the configuration is pushed up along the corresponding eigenvector while forces are minimized in the perpendicular hyperplane.

This procedure brings the structure to the associated first-order saddle point, converging with any desired precision. (3) When the saddle point is reached, a step of energy minimization is performed in order to bring the configuration into a new minimum.

B. Coupling ART nouveau and DFT

Until now, ARTn has been mostly employed with empirical potentials or local-basis *ab initio* codes such as SIESTA³⁹ and BigDFT.³⁶ For the present study, such level of description is insufficient since known empirical potentials cannot take into account the complex chemistry of oxidation reaction and associated rearrangement. We therefore select to use the plane-wave DFT VASP^{37,38} code and interfaced this widely used package directly with the ARTn code.⁵⁶

ARTn code finds a saddle point around a local minimum by following the eigenvector associated at one negative eigenvalue of the hessian matrix. The search for a negative eigenvalue occurs by iteration using the Lanczos algorithm. In this approach, at each iteration, Lanczos calls VASP code to calculate the atomic forces from different configurations (Fig. 1). The use of DFT increases the physical accuracy during the Minimum Energy Path (MEP) search and allows atomic scale chemical reaction to occur, generating a reliable energy landscape description even for transition points. The MEP search procedure can be summarized as follows: from a given relaxed state obtained by VASP configuration optimization with VASP, ARTn searches for a MEP, where forces of each step along the MEP are estimated from a single point calculation using VASP. Once the saddle point is obtained, the configuration is relaxed into a new minimum using VASP. Due to ARTn's efficiency, only a few hundred force evaluations are necessary to generate an event, i.e., converging to a saddle point from a local minimum and relaxing into a new nearby state.³⁶

C. Details of DFT calculations

The generalized gradient approximation of Perdew-Burke-Ernzerhof is used as exchange and correlation energy functional.⁴⁵ We use PAW pseudopotentials for the silicon,

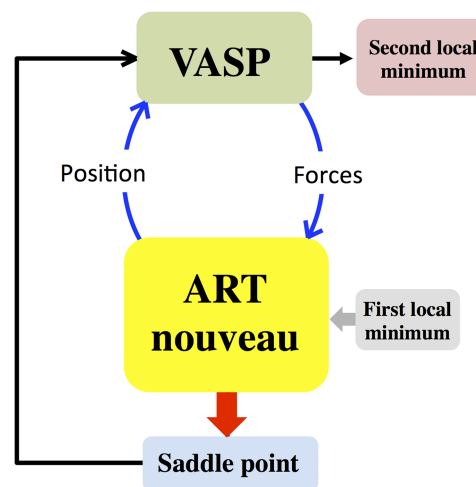


FIG. 1. ARTn-VASP coupling procedure.

oxygen, and hydrogen atoms.^{46,47} The plane wave energy cut-off is fixed at 400 eV, and the Γ point is used to sample the Brillouin zone. The spin polarization is taken into account to describe adequately the oxygen molecule and its spin conversion. In all our calculations, the oxygen molecule is free to relax and the spin is free to convert.

D. Simulation cell

The Si(100) surface is modeled as a repeated $\text{Si}_{224}\text{H}_{32}$ slab with a $p(2 \times 2)$ reconstruction on the surface. The cell is formed with fourteen layers of sixteen silicon atoms [Fig. 2(a)]. The surface contains eight dimer units. Hydrogen atoms are placed to passivate the dangling bonds of the silicon atoms below the slab. The seven bottom layers of the slab and hydrogen atoms are kept fixed to simulate the bulk, all other atoms are free to relax. A vacuum zone of 15 Å is introduced above the surface.

The objective of this study is to investigate the thermal oxidation process beyond the oxidation of the silicon topmost layer. The oxidized surface model has been constructed as reported in the literature and based on our previous results.^{16,17,43,44} We modeled partially and fully oxidized surfaces by adsorbing sixteen or thirty two oxygen atoms, respectively, using an elementary pattern that can be depicted as alternate 4-O atom and 6-O atom rings as shown in Figs. 2(b) and 3. This atomic scheme is observed as a favorable oxidized configuration for the silicon surface in several works and represents a well-characterized starting point.^{21,44,48,49} In the following, we label the subsurface area between the uppermost oxidized layer and atomic layers below as surface-1, surface-2, and surface-3 layers, following Fig. 2(f). The atomic positions for these initial configurations are directly derived from the output of the calculations described in our previous

papers,^{16,17} where the 4-O-atom ring is characterized by an Adjacent Dimer Bond (ADB) as described in Ref. 16. Considering our slab size, the partially oxidized surface contains two 6-O atom rings [Figs. 2(b) and 3(a)] and two 4-O atom rings, and the fully oxidized surface contains four 6-O atom rings and four 4-O atom rings [Figs. 3(b) and 3(c)]. In the following, we use a 4/6 O ring pattern to refer to alternate 4-O atom and 6-O atom rings.

E. Simulation of the adsorption reaction of oxygen molecule

The alternate 4/6 O ring elementary pattern used as an oxidized surface model exhibits only few reactive sites for the adsorption of a new oxygen molecule: on this surface, several adsorption sites as a function of surface topology were investigated (not detailed here), and only the 6-O ring appears [dashed hexagons on Figs. 2(b) and 3] as a reactive site as it is wide enough to allow adsorption and further insertion of dioxygen molecules into the surface.

For this study, we proceed as follows: initially a dioxygen molecule is positioned at 2 Å above a 6-O ring adsorption site and its configuration relaxed with VASP. Adsorption of one to two dioxygen molecules is performed in each adsorption 6-O ring site to simulate increasing coverage on the partially oxidized surface. Adsorption of one to four dioxygen molecules is performed in each adsorption 6-O ring site on the fully oxidized surface to simulate increasing coverage on a fully oxidized surface (see Fig. 3, due to the periodic condition, only one 6-O ring adsorption site on configuration A and two 6-O ring adsorption sites are visible on configurations B and C). Atomic diffusion into the interfacial subsurface area from each resulting configuration is then analyzed with ARTn-VASP.

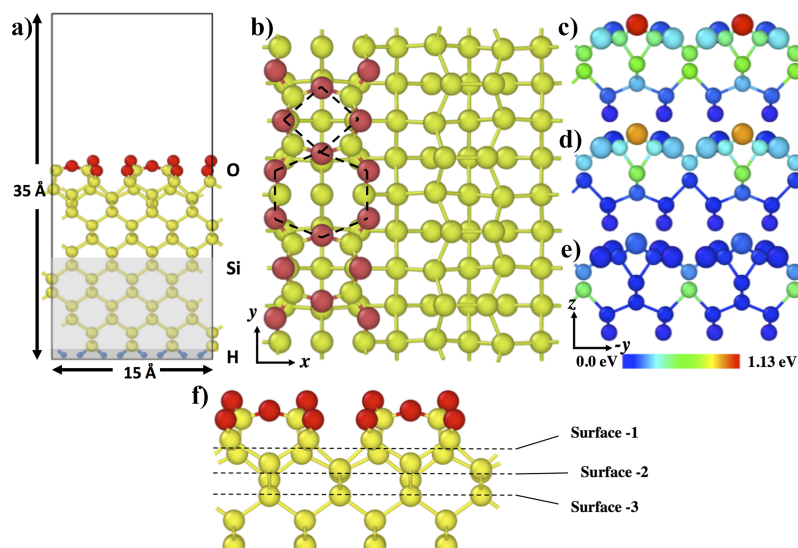


FIG. 2. (a) Side view (xz plane) of the simulation cell ($\text{Si}_{224}\text{H}_{32}\text{O}_{32}$). The topmost silicon atoms (yellow spheres) of the slab are fully oxidized (oxygen atoms in red spheres). (b) Top view of the Si(100) surface where only one row of dimers is oxidized: on the right, the (2×1) reconstruction on the row of dimers is visible, and on the left, the dotted black lines highlight the alternating 6-O atom and 4-O atom rings used as the elementary pattern in this study. The dashed square corresponds to the 4-O ring and the dashed hexagon to the 6-O ring. The adsorption site is located into the 6-O rings. (c)–(e) are side views (yz plane) with a color range used to quantify the total strain energy per atom in (c) calculated using Eq. (2). This total strain energy can be decomposed as angular distortion [shown in (d)] and stretches strain energy [shown in (e)] contributions. In (c)–(e), the larger spheres correspond to oxygen atoms and smaller ones refer to silicon atoms. x , y , and z directions correspond to $[110]$, $[-110]$, and $[001]$, respectively. (f) is a side view of the silicon slab where the description of subsurface layers used in the paper is provided.

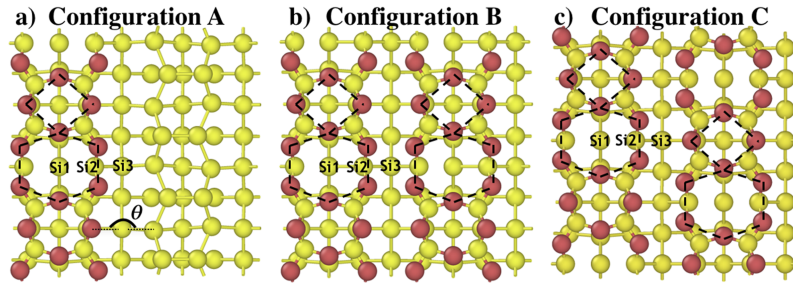


FIG. 3. Top views of the three surface oxidation configurations used here and exhibiting the elementary 4O/6O pattern as described in Fig. 2(b). (a) The surface is half covered using two elementary patterns on a single row of dimers, (b) and (c) the silicon surface is fully oxidized arranged symmetrically and antisymmetrically compared to the channel axis, respectively. Structures (b) and (c) have an energy difference of -0.95 eV in favor of (c). At the interface, we identify Si1, Si2, and Si3 silicon atoms: Si1 is the silicon atom below the row of dimers in the middle of the 6-O ring in the surface-2 layer, Si2 is the silicon atom on the side of the 6-O ring in the surface-1 layer, and Si3 is the silicon atom in the channel in the surface-2 layer.

F. Adsorption energies and strain energy calculations

The adsorption energy of the dioxygen molecule in Sec. III B is calculated according to the following:

$$E_{ads} = E_{O_2 ads on ox model} - (E_{ox model} + E_{O_2}), \quad (1)$$

where $E_{O_2 ads on ox model}$ corresponds to the total energy of the adsorbed oxygen molecule on the oxidized surface model, $E_{ox model}$ is the total energy of the oxidized surface model containing sixteen or thirty two oxygen atoms depending on the considered partially and totally oxidized surface model, respectively, and E_{O_2} is the energy of an isolated oxygen molecule.

In the following, we discuss the variation of the total strain energy of the system and the atomic strain energy for local characterization. For convenience, we use the Valence Force Field (VFF) approach^{53,55} that considers the variation of the total energy through two contributions: one comes from the variation of the suboxide energy (ΔE_{subox}) and the second part is related to the variation of the strain energy variation (ΔE_{strain}). The Keating formalism⁵⁰ is used to evaluate the local strain and has been widely used for studying the SiO₂/Si(001) interface.^{51–55} The strain energy (E_{strain}) is taken to be zero for a perfect structure (Si bulk or SiO₂ bulk) and positive for any deviation from the perfect structure

$$E_{strain} = \frac{1}{2} \sum_i k_b (b_i - b_0)^2 + \frac{1}{2} \sum_{ij} k_\theta (\cos \theta_{ij} - \cos \theta_0)^2, \quad (2)$$

where k_b (in eV/Å²) and k_θ (in eV) are the constants associated with bond stretching and angle distortion, respectively. b_i and b_0 (in Å) represent the bond length of the i th bond and its equilibrium distance, and θ_{ij} and θ_0 are the angle between the i th and j th bonds and its equilibrium angle, respectively. The Keating parameters used for Eq. (2) are issued from Table I [KT(s-h) parameters] in Ref. 55 where these data are fitted on the energy calculated using DFT calculation for the Si/SiO₂ interface after removing the suboxide part. In this model, we do not consider the oxygen-oxygen bond. The total strain energy is obtained by summing over all bonds. In the following, we use ΔE_{strain} as the E_{strain} difference between two configurations.

An atomic strain energy can be defined and assigned to each atom by projecting half of each bond contribution onto a given O or Si atom. This atomic strain energy parameter is used

throughout the paper to help understand the propagation front of the oxidation process. These values are put in relation with activation barrier changes in the results section (Secs. III C and IV). In Fig. 2(c), the estimated strain concentration in the three topmost layers at the interface is shown. By decomposing the total strain energy, two strained domains appear: the first one where the strain is dominated by the angular distortion, due to the angle on the silicon atom beneath the ADB close by -42.0° compared to 109.47° (tetrahedral angle) and to the angle Si–O–Si formed by the ADB in the 4-O ring which decrease to -82.1° compared to the equilibrium angle (180°) [Fig. 2(d)] and a second domain where the strain is due to the Si–Si bond stretching [Fig. 2(e)] beneath the 6-O ring in the row of dimers [$d(\text{Si–Si}) = 2.49\text{--}2.50$ Å, compared to 2.36 Å in the silicon bulk]. The identified 6-O ring adsorption site in this structure corresponds to a tensile strain domain.

The ARTn-VASP MEP search procedure is performed to investigate the diffusion mechanism of the oxygen atom at the interface. In spite of the large number of events generated, we cannot assume a complete set, however, previous experience with ARTn and analysis of the found mechanisms suggest that we identify some major diffusion pathways. To facilitate reading, we focus here only on typical mechanisms associated with the propagation of the oxidation front at the Si/SiO₂ interface; the full list is available upon request.

III. ATOMIC INSIGHT OF THE PROPAGATION OF THE OXIDATION FRONT AT THE Si/SiO₂ INTERFACE: ADSORPTION AND SUBSEQUENT DIFFUSIONS

A. Initial strain in oxidized surface-models

To study the environment and local strain effect on diffusion mechanisms, three surface coverage models are used as shown in Fig. 3. These surfaces are distinguishable by their 6/4 O ring pattern distribution on the surface. A low coverage is modeled with only one oxidized row of dimers (configuration A), and two fully oxidized surfaces are considered where the two row of dimers can be oxidized with a symmetric 6/4 O ring pattern distribution considering the channel axis (configuration B) and antisymmetric distribution (configuration C). In the following, local structure deformation in each configuration is discussed by providing the atomic strain energy on key atoms from the interface.

Oxidized or not, rows of dimers are connected by a silicon atom in the channel called Si3 in Fig. 3. The strain on the Si3 atom depends on whether Si3 is connected to a 6-O ring, a 4-O ring, or a non-oxidized row. This strain is related to the angular deformation associated with the ring size: in configuration A, the strain energy on 6-O-ring Si3 is only 0.02 eV with $\theta = 105.5^\circ$, while it is four times higher at 0.08 eV with $\theta = 123.8^\circ$ on Si3 linked to the 4-O ring. A similar but less important strain difference is observed in configuration B with the strain energy going from 0.10 to 0.12 eV between the two rings. In this configuration, the juxtaposition of the same types of rings emphasizes the compressive effect on the environment of the 6-O ring with $\theta = 93.8^\circ$ by opposition to the tensile effect of the 4-O ring with $\theta = 128.3^\circ$. Because of symmetry, no strain difference is observed for Si3 between the two rings in configuration C: in both cases, the strain energy is 0.04 eV with $\theta = 112.1^\circ$, close to the tetrahedral equilibrium angle ($\theta_0 = 109.5^\circ$).

Elastic deformation can also take place through bond stretching below the row of dimers on Si1–Si2 and Si2–Si3 between surface-1 and surface-2 layers. Si1–Si2 and Si2–Si3 bond lengths are 2.56 Å and 2.37 Å, respectively, in configurations A and C and 2.41 Å and 2.31 Å in configuration B, which can be explained by the compressive effect of the 6-O ring, more important in B than in A and C. Thus, the main contribution of the stretch deformation in the strain energy comes from the Si–Si bonds located below the row of dimers.

B. Adsorption of O₂ molecule

As mentioned previously in Sec. II E, adsorption of oxygen molecules is conducted on the 6-O ring site as it appears to be the only reactive site at large coverage. Assuming this, we investigate two successive molecular oxygen adsorptions on the two 6-O rings of configuration A and four successive O₂ adsorptions on the four 6-O rings of configurations B and C. Adsorptions on B and C are conducted by sequentially filling one row of dimers before oxidizing the second row.

Throughout this paper, we use the following notation: A1 and A2; B1, B2, B3, and B4; and C1, C2, C3, and C4 to refer to increasing O₂ deposition on a given configuration. A1 corresponds to the structure obtained after a single adsorption on configuration A, B3 is the adsorbed configuration after the deposition of three oxygen molecules on starting configuration B, and C2 is the adsorbed configuration after the deposition of two oxygen molecules on starting configuration C.

After each deposition, the oxygen molecule penetrates beneath the surface oxidized layer through the 6-O ring and oxidizes the Si–Si bonds below the row of dimers between the surface-1 and the surface-2 layers. Adsorption energies (E_{ads}) and variations of strain energies calculated considering all the atoms of the simulation cell (ΔE_{strain}) are reported in Table I. The adsorption vs. variation of strain energies are plotted in Fig. 4(a) and the corresponding configurations in Fig. 4(b). The plot clearly shows a linear relationship between these two energies. This result validates the used approach that consists in the separation of total energy in two contributions: the energy of the suboxide and the strain energy. Here, the variation of

TABLE I. Strain energy changes (ΔE_{strain}) induced by oxygen molecule adsorption calculated according to Eq. (2), and oxygen molecule adsorption energies (E_{ads}) [Eq. (1)] for selected adsorbed configurations. Some of these configurations are shown in Fig. 4(b).

	ΔE_{strain} (eV)	E_{ads} (eV)
A1	−1.34	−8.97
A2	−1.00	−8.85
B1	−0.53	−8.48
B2	−0.14	−8.48
B3	1.45	−7.72
B4	1.14	−7.81
C1	−1.23	−8.95
C2	−1.02	−8.84
C3	−0.97	−8.75
C4	−0.55	−8.71

the suboxide energy during the adsorption is −8.36 eV, and the strain energy contributes to the total energy with a proportional coefficient calculated to be 0.46.

These adsorbed configurations are the starting configurations for interfacial diffusion in the surface-2 layer and toward

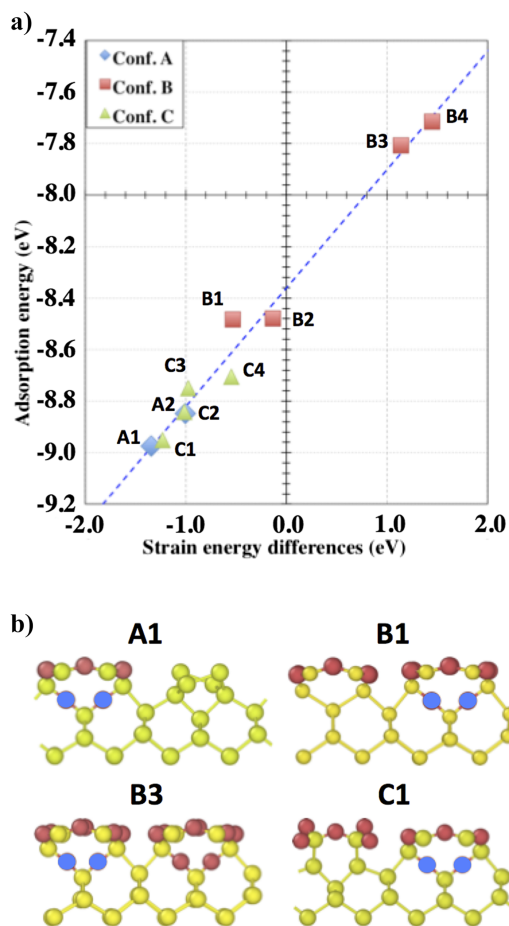


FIG. 4. (a) Adsorption energies as a function of strain energy change due to oxygen molecule adsorption. Values are given in Table I. The fit corresponding to the dashed line is $y = 0.46x - 8.36$. (b) Side view in the (xz) plane of selected different configurations to be analyzed with ARTn-VASP coupling where the number associated with the configuration letter indicates the number of adsorbed additional oxygen molecules. In blue, the new adsorbed oxygen atoms are highlighted.

the deeper layer resulting in the oxidation of the Si–Si bond between surface-2 and surface-3 layers, i.e., at the growing Si/SiO₂ interface.

Comparing configurations A and C, we note that the increase in the oxygen coverage decreases the overall configuration strain thanks to oxygen atoms that insert into the Si–Si bonds beneath the row of dimers: the Si–Si bonds that are initially strongly stretched (2.50–2.56 Å depending on the considered configuration compared to the 2.37 Å in bulk silicon) relax, thanks to the formation of Si–O bonds of 1.63 Å, close to the characteristic Si–O bonds of silica (1.61 Å). Atomic strain energy calculations reveal that stretching contribution surrounding atom Si1 below the row of dimers decreases from 79% to 0% when evolving from the Si–Si bond to Si–O bond on both configurations A or C. Same tendency has been observed for Si2 from 40% to 10%. Furthermore, the oxygen adsorption widens the 6-O ring.

For configuration B, the silicon atom in the channel (Si3) and below the row of dimers (Si1) becomes even more compressed at each adsorption with the atomic strain energy increasing at each adsorption. This tendency is reflected in total strain energy given in Fig. 4(a) where it increases with coverage. This shows how the strain is allocated along the silicon-oxygen chain with maximum strain variation on Si1 with the change of local environment while Si2 strain energy remains stable.

C. Activated O diffusion at the SiO₂/Si interface

We now focus on the oxygen atom diffusion starting from four selected configurations—A1, B1, B3, and C1, looking more specifically at atomistic mechanisms enabling the diffusion front to progress. These four configurations have been chosen since they differ significantly in terms of energy barriers and energy gains. Since mechanisms obtained from A1 and A2, B1 and B2, B3 and B4 or C1 to C4 are energetically very similar, we chose not to repeat the discussion for diffusion from A2, B2, and B4 and C2, C3, and C4. Among the diffusion pathways identified by ARTn, we leave aside about 10 local mechanisms characterized by too high activation barriers or local mechanisms leading to final states less stable than the initial state, irrespective of the coverage. Note that a mechanism not favored at low coverage can become favorable with increasing coverage and vice versa.

Diffusion pathways are investigated as a function of oxygen coverage. For clarity, we discuss only mechanisms that enable the oxidation front to propagate, i.e., those associated with the lowest activation barriers or that allow the system to stabilize. For the selected diffusion pathways, we establish a correlation between the activation barriers and energy gains along the diffusion pathway and the strain energy accumulated in the substrate.

In Fig. 5, we present O diffusion mechanisms at the interface obtained with ARTn-VASP from configurations A1, B1, B3, and C1. The configurations obtained after O diffusion in these structures are provided in Fig. 5(a), and a schematic view of these diffusion pathways is given in Fig. 5(b). The same final structural configurations obtained from the different starting configurations are referred by the same unique tag in Fig. 5(a). For instance, the final configuration #2 can be

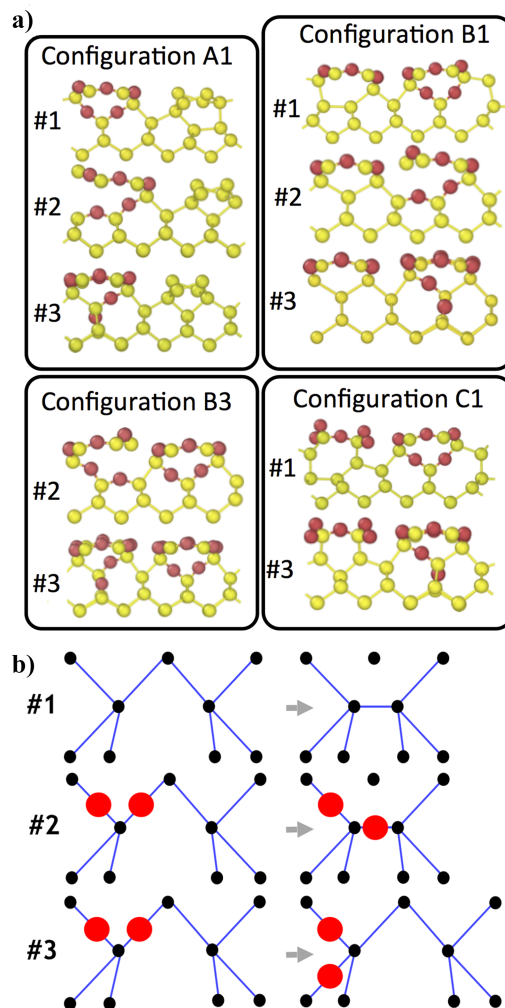


FIG. 5. (a) Final configurations obtained with ARTn-VASP coupling obtained from initial configurations A1, B1, B3, and C1. Same final structural configurations obtained from different starting configurations are referred to using the same label. A1, B1, C1, and B3 do not correspond to the same oxygen coverage. (b) Schematic representation of three described diffusions obtained with ARTn-VASP coupling.

obtained from A1, B1, and B3, independently of the coverage and will be designed as A1-#2, B1-#2, and B3-#2, respectively. To be consistent with this notation, the diffusion mechanism leading to such final configurations will be referred to as diffusion mechanism #2. Same rules are applied to mechanisms #1 and #3.

These three favorable diffusion pathways involve predominantly either Si or O [Fig. 5(b)]. Mechanism #1 can be described as the diffusion of a silicon atom into the surface-2 layer resulting in a reconstruction at the interface, with the formation of a Si–Si dimer. In #2, the oxygen atom located beneath the 6-O ring between surface-1 and -2 layers oxidizes the silicon atom in the channel, resulting in an oxidized Si–Si dimer at the interface through formation of a Si–O bond with the Si3 atom. In #3, an oxygen atom diffuses deeper into the bulk starting from between surface-1 and surface-2 layers to end between surface-2 and surface-3 layers.

The various energy variables associated with these diffusion mechanisms [activation energy (E_{ac}) and relative stability (dE) calculated as the difference of the total energy between

TABLE II. Mechanisms obtained with ARTn-VASP coupling from configurations A1, B1, B3, and C1. Numbers correspond to events presented in Fig. 5. For each mechanism, we show the activation energy (E_{ac}), the relative stability (dE), and the total displacement perpendicular to the surface along the z -axis of the event (dz).

Event	E_{ac} (eV)	dE (eV)	dz (Å)
A1-#1	1.21	0.17	3.06
A1-#2	1.46	0.87	3.98
A1-#3	2.96	0.49	-0.52
B1-#1	3.42	-0.80	4.54
B1-#2	0.89	0.50	3.82
B1-#3	2.77	0.20	-0.60
B3-#2	0.63	-0.28	4.22
B3-#3	1.80	0.04	-0.77
C1-#1	2.57	1.39	2.89
C1-#3	3.22	0.49	-1.27

the initial state and the final state of the diffusion mechanism] are given in Table II. E_{ac} ranges from a relatively low 0.63 to 3.42 eV, corresponding to an unlikely diffusion at usual deposition temperatures. Negative values for dE indicate the stabilization of the system. Note that when dE is close to 0, the two configurations have the same probability to exist, from a thermodynamical point of view. For most events, the global atomic displacement perpendicular to the surface (dz), calculated as the sum of the displacement of all the atoms along the z -axis, is positive, which indicates a surface swelling up as atoms diffuse towards the bulk.

It is interesting to detail a few of these events. From A1, corresponding to a low coverage in oxygen species, both pathways #1 and #2 involve accessible barriers with an advantage for #1, with $E_{ac} = 1.21$ eV. The same mechanism #1, starting from B1 and C1 and leading to configurations B1-#1 and C1-#1, is less probable, associated with significantly higher activation energies ($E_{ac} = 3.42$ eV and 2.57 eV, respectively). Since configuration A1-#1 shows a total energy close to that of the initial state ($dE = 0.17$ eV), the interface reconstruction by Si-Si dimer creation is thus a favorable mechanism at low coverage.

For the fully oxidized B1, even though it requires crossing high energy barriers, configuration B1-#1 associated with the interface reconstruction in a non-oxidized area below the

row of dimers appears clearly as the most thermodynamically favorable with an energy -0.80 eV below that of the initial state. By comparison, B1-#2, with $dE = 0.50$ eV, is less stable but can be accessed more easily from a kinetic point of view with a 0.89 eV barrier.

Note here that as the coverage increases, the activation barrier of the pathway #2 lowers from A1 to B1 and to B3 barriers falls from 1.46 to 0.89 and 0.63 eV, respectively, while the final state gains in stability: with $dE = -0.28$ eV, for B3-#2, 0.78 eV below B1-#2 and 1.08 eV below A1-#2. A similar trend is observed for pathway #3, where B3-#3 is more stable by 0.16 eV with respect to B1-#3, and for pathway #1: $dE = -0.80$ eV for B1-#1 and 0.17 eV for A1-#1.

This suggests that an unlikely diffusion event at low coverage can become the dominant mechanism at the higher coverage, enabling the oxidation front to progress, as local strain evolves.

ARTn-VASP does not identify any mechanism from C1 that would lead to a configuration similar to configuration #2. Generated pathways are rather characterized by high activation energies associated with a much slower kinetics.

These results suggest that oxygen coverage is a dominant factor for oxidation at the Si/SiO₂ interface: a configuration that is initially unfavourable energetically becomes favored at higher coverage. This observation confirms what had already been seen at very low coverage:¹⁶ the silicon surface adapts to the presence of oxygen species. At low coverage, silicon atoms are likely to diffuse at the interface leading to the interface modification during the growth; Si-Si bonds that are weaker than Si-O bonds break first to reconstruct the interface. As the surface becomes fully oxidized, oxygen atom diffusion is favored due to the accumulated strain.

IV. DISCUSSION: STRAIN-DRIVEN DIFFUSION PROCESS

We can correlate the various diffusion mechanisms with the evolution of the strain energy in the system. This correlation is presented for mechanism #2 (A1-#2, B1-#2, and B3-#2) in Fig. 6 and for mechanism #3 (A1-#3, C1-#3, B1-#3, and B3-#3) in Fig. 7.

Figure 6 describes the mechanism #2 associated with an oxygen diffusing in the surface-2 layer from structures A1,

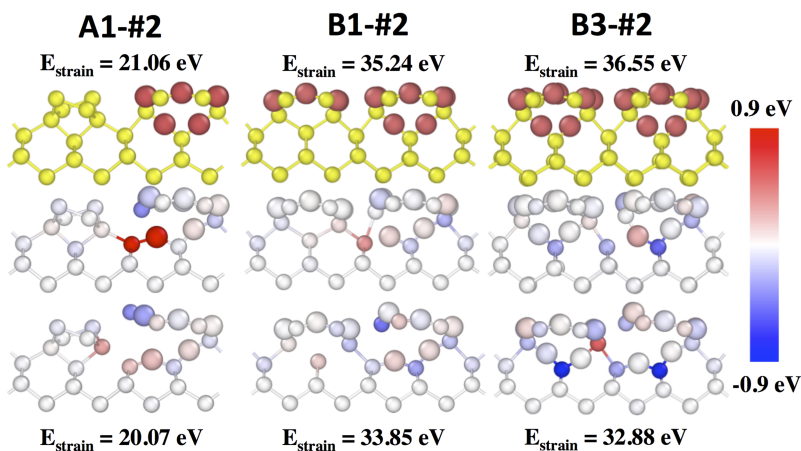


FIG. 6. Diffusion path #2 from A1 (left), B1 (middle), and B3 (right). From top to bottom, initial configuration, the saddle point, and final state are provided. The color for the saddle point and final configuration represents the atomic strain energy difference with initial configuration calculated with Eq. (2). The strain energy ranges from -0.90 eV to 0.90 eV, and its color scale is given on the right. The total strain energy of the initial and final configurations is given above and below the structures. The oxygen atoms are represented in red or by large spheres and silicon atoms in yellow or by little spheres.

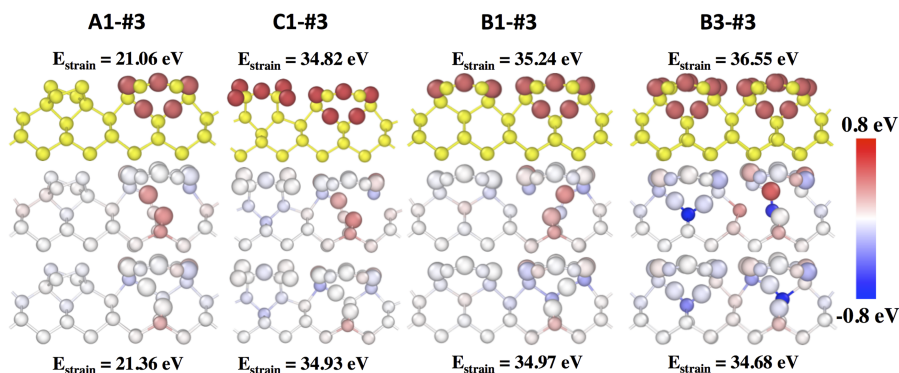


FIG. 7. Left to right: Diffusion mechanism #3 from A1, C1, B1, and B3 configurations, respectively. From top to bottom, the initial configuration, saddle point, and final state are provided. The colors for the saddle point and final configuration represent the atomic strain energy difference with initial configuration calculated with Eq. (2). The associated strain energy ranges from -0.80 eV to 0.80 eV and is colored according to the scale on the right. The total strain energy of the initial and final configurations is given above and below the structures. The oxygen atoms are represented in red or by large spheres and silicon atoms in yellow or by little spheres.

B1, and B3 (up). The atomic strain energy is highlighted at the saddle point (middle) and for the final configurations A1-#2, B1-#2, and B3-#2 (down) as a difference with the respective starting structures.

As discussed in Sec. III C, the activation energy decreases as the oxygen coverage increases and the sub-surface oxidation progresses (Table II). The final state in A1 with the Si2 silicon atom pointing upward differs from the final states of B1 and B3 where the silicon atom points downward because of the presence of the 6-O ring in the vicinity. This explains the barrier, probably electrostatic, of around 0.20 eV to flip silicon atoms into a configuration where it points upward in the final states B1 and B3.

More crucially, however, this trend can be correlated with a reduced strain on the diffusing oxygen atom at the saddle point and on the silicon atom in the channel at the final state. For the densest coverage, configuration B3, the Si1 silicon atom relaxes at the interface Si/SiO₂ as soon as diffusion is initiated, and only the diffusing oxygen exhibits a significant atomic strain energy. This occurs as the total strain energy goes up from 21.06 eV for A1 to 35.24 eV for B1 and 36.55 eV for B3. In B3, the strain stored in the interfacial layer is such that an atomic rearrangement becomes necessary to relax the accumulated strain and reduces structural deformations. The presence of strain therefore lowers activation energies, facilitating diffusion and leading to the stabilization of the system. Stored strain energy, therefore, catalyzes O diffusion.

This conclusion is supported by the similar trends observed for mechanism #3 presented in Fig. 7: as the total strain energy increases from 21.06 eV in A1 to 34.29 eV, 35.24 eV, and 36.55 eV for C1, B1, and B3, respectively, the activation energy decreases from 3.48 eV in A1 to 3.22 eV, 2.77 eV, and 1.80 eV, respectively, while final states are stabilized with respect to the initial configurations with $dE = 0.52$ eV, 0.49 eV, 0.20 eV, and 0.04 eV, respectively.

The activation energies and relative stabilities indicated in Table II are plotted in Fig. 8 as a function of strain energy change (ΔE_{strain}) between the saddle (E_{ac}) or final state (dE) and initial state, respectively. These values are intimately correlated to the initial strains and to their relaxation. The trend

observed in Fig. 8 is similar to the one observed between the adsorption energies and the strain energy changes shown in Fig. 4(a).

The strain, therefore, acts like an energy reservoir that can be drawn up during atomic diffusion and shifting the energy balance of various diffusion mechanisms. The higher the initial strain, the lowest E_{ac} and dE become, favoring oxygen insertion. This accumulated strain is directly linked to the interfacial environment, i.e., to the oxygen coverage and to the oxidation state in a sub-surface. We see, in particular, that the strain energy stored at the interface as the oxidation progresses, i.e., for increasing coverage, drives the atomic diffusion. These results are consistent with a layer-by-layer growth mode during silicon thermal oxidation.^{6,8}

No kinetically relevant diffusion mechanisms were observed from configuration C1. All identified pathways are associated with high activation barriers and energetically

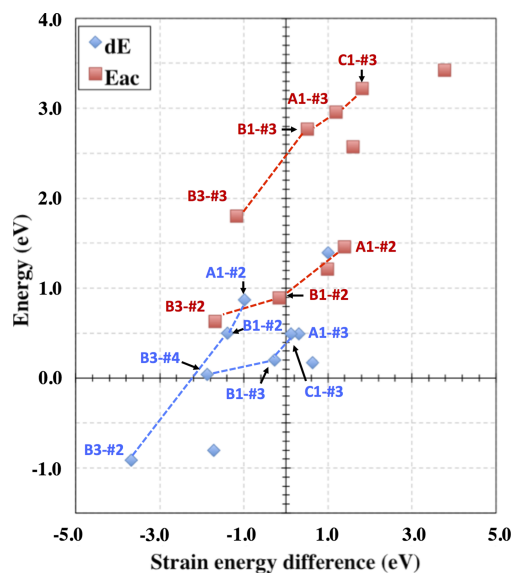


FIG. 8. Correlation between the energetic parameters of the diffusion mechanism as a function of strain energy differences between initial and final configurations (dE) and initial and saddle point configurations (E_{ac}), respectively. Dashed lines are a guide for the eye.

unfavorable final configurations. This illustrates the high stability of configuration C already discussed before. The 4-O and 6-O ring proximity on either sides of the channel reduces strain effects whereas configuration B increases them. However, while the correlation between strain building and layer-by-layer growth is clear for the systems studied here, it will be necessary to evaluate the effects at the large scale of oxide nanostructuring on the diffusion kinetics of oxidation front through the mesoscopic modeling approach, such as kinetic Monte Carlo,¹⁵ while introducing the strain effect.

V. CONCLUSION

The oxidation mechanisms of sub-surface silicon (100) have been investigated using a coupling of ARTn-VASP methodologies. Different surface coverage with a 4/6 O ring pattern was studied in order to understand the effect of the local environment on oxygen adsorption and diffusion at the interface. The environment effect was discussed in terms of strain energy thanks to the Keating model. The oxygen molecule adsorption energy shows a linear dependence with strain energy. Furthermore, the interface diffusions obtained exhibit also a close correlation with strain at the Si/SiO₂ interface as the oxidation progresses. We have shown that the interface reconstructions are rapidly favorable and that the oxidation of deep layers occurs when the oxygen surface coverage is sufficiently important. The strain energy accumulated at the interface will favor atomic diffusions energetically at high coverage which were not allowed at low coverage. The strain accumulation in the structure decreases the activation energies and inverses the relative stability of final configurations. A progressive increasing strain in the system changing the trend and the feasibility of diffusion to occur at the Si/SiO₂ interface is consistent with a layer-by-layer scheme of the silicon oxidation process.

The results presented here offer a clear picture for the first stage of oxidation: the built-up strain, as the surface oxidizes, should accelerate the diffusion of oxygen. As the interface grows, however, the disordered SiO₂ network should allow the strain to relax, which will slow the progression to a halt. This second phase remains to be characterized.

ACKNOWLEDGMENTS

This work has been performed using CALMIP (Grant Nos. 1552 and 1418), IDRIS (Grant No. 100588), and Curie (Grant No. gen7474) computer resources. We also thank Calcul Québec/Compute Canada for computer time. The project has been funded in part by the Axe Amérique du Nord from Université Paul Sabatier and Université de Montréal.

¹R. G. Arns, *Eng. Sci. Educ. J.* **7**, 233 (1998).

²T. Zhu and M. N. Chong, *Nano Energy* **12**, 347 (2015).

³R. Jansen, *Nat. Mater.* **11**(5), 400 (2012).

⁴M. T. Bohr, R. S. Chau, T. Ghani and K. Mistry, *IEEE Spectrum* **44**, 29 (2007).

⁵J. H. Oh, H. W. Yeom, Y. Hagimoto, K. Ono, M. Oshima, N. Hirashita, M. Nywa, A. Toriumi, and A. Kakizaki, *Phys. Rev. B* **63**, 205310 (2001).

⁶S. Ogawa, A. Yoshigoe, S. Ishidzuka, Y. Teraoka, and Y. Takakuwa, *Jpn. J. Appl. Phys., Part 1* **46**, 3244 (2007).

⁷S. Ogawa and Y. Takakuwa, *Jpn. J. Appl. Phys., Part 1* **45**, 7063 (2006).

⁸S. Ogawa, J. Tang, A. Yoshigoe, S. Ishidzuka, Y. Teraoka, and Y. Takakuwa, *Jpn. J. Appl. Phys., Part 1* **52**, 110128 (2013).

⁹S. Ogawa, J. Tang, and Y. Takakuwa, *AIP Adv.* **5**, 087146 (2015).

¹⁰H. Z. Massoud, J. D. Plummer, and E. A. Irene, *J. Electrochem. Soc.* **132**, 2685 (1985).

¹¹E. Kobeda and A. Irene, *J. Vac. Sci. Technol., B: Microelectron. Nanometer Struct.* **7**, 163 (1989).

¹²J. T. Fitch, C. H. Bjorkman, and G. Lucovsky, *Appl. Surf. Sci.* **39**, 103 (1989).

¹³A. Hemeryck, N. Richard, A. Estève, and M. Djafari Rouhani, *Surf. Sci.* **601**, 2082 (2007).

¹⁴A. Hemeryck, N. Richard, A. Estève, and M. Djafari Rouhani, *Surf. Sci.* **601**, 2339 (2007).

¹⁵A. Hemeryck, A. Estève, N. Richard, M. Djafari Rouhani, and G. Landa, *Surf. Sci.* **603**, 2132 (2009).

¹⁶A. Hemeryck, A. Estève, N. Richard, M. Djafari Rouhani, and Y. J. Chabal, *Phys. Rev. B* **79**, 035317 (2009).

¹⁷A. Hemeryck, A. Mayne, N. Richard, A. Estève, Y. J. Chabal, M. Djafari Rouhani, G. Dujardin, and G. Comtet, *J. Chem. Phys.* **126**, 114707 (2007).

¹⁸N. Mousseau, L. K. Bélan, P. Brommer, J.-F. Joly, F. El-Mellouhi, E. Machado-Charry, M.-C. Marinica, and P. Pochet, *J. At., Mol., Opt. Phys.* **2012**, 14.

¹⁹T. Akiyama and H. Kageshima, *Surf. Sci.* **576**, L65 (2005).

²⁰L. Colombi and M. C. Payne, *Phys. Rev. Lett.* **95**, 196101 (2005).

²¹T. Yamasaki, K. Kato, and T. Uda, *Phys. Rev. Lett.* **91**, 146102 (2003).

²²A. Bongiorno and A. Pasquarello, *Phys. Rev. Lett.* **88**, 125901 (2002).

²³A. Bongiorno and A. Pasquarello, *J. Mater. Sci.* **40**, 3047 (2005).

²⁴K. Shiraishi, H. Kageshima, and M. Uematsu, *Jpn. J. Appl. Phys., Part 2* **39**, L1263 (2000).

²⁵H. Kageshima and K. Shiraishi, *Phys. Rev. Lett.* **81**, 5936 (1998).

²⁶H. Watanabe, T. Baba, and M. Ichikawa, *Jpn. J. Appl. Phys., Part 1* **39**, 2015 (2000).

²⁷T. Akiyama, T. Ito, H. Kageshima, and M. Uematsu, *Phys. Rev. B* **77**, 115356 (2008).

²⁸R. J. Jaccodine and W. A. Schlegel, *J. Appl. Phys.* **37**, 2429 (1966).

²⁹A. Korkin, J. C. Greer, and G. Bersuker, *Phys. Rev. B* **73**, 165312 (2006).

³⁰X. L. Han, G. Larrieu, and C. D. Krzeminski, *Nanotechnology* **24**, 495301 (2013).

³¹C. D. Krzeminski, X. L. Han, and G. Larrieu, *Appl. Phys. Lett.* **100**, 263111 (2012).

³²P. F. Fazzini, C. Bonafos, A. Claverie, A. Hubert, T. Ernst, and M. Respaud, *J. Appl. Phys.* **110**, 033524 (2011).

³³G. T. Barkema and N. Mousseau, *Phys. Rev. Lett.* **77**, 4358 (1996).

³⁴R. Malek and N. Mousseau, *Phys. Rev. E* **62**, 7723–7728 (2000).

³⁵E. Machado-Charry, L. K. Béland, D. Caliste, L. Genovese, N. Mousseau, and P. Pochet, *J. Chem. Phys.* **135**, 034102 (2011).

³⁶G. Kresse and J. Furthmüller, *Phys. Rev. B* **54**, 11169 (1996).

³⁷G. Kresse and D. Joubert, *Phys. Rev. B* **59**, 1758 (1999).

³⁸L. J. Munro and D. J. Wales, *Phys. Rev. B* **59**, 3969 (1999).

³⁹G. Henkelman and H. Jónsson, *J. Chem. Phys.* **111**, 7010 (1999).

⁴⁰N. Mousseau and G. T. Barkema, *Phys. Rev. E* **57**, 2419 (1997).

⁴¹F. El Mellouhi, N. Mousseau, and P. Ordejon, *Phys. Rev. B* **70**, 205202 (2004).

⁴²P. Ganster, L. K. Béland, and N. Mousseau, *Phys. Rev. B* **86**, 075408 (2012).

⁴³F. Fuchs, W. G. Schmidt, and F. Bechstedt, *Phys. Rev. B* **72**, 075353 (2005).

⁴⁴J. P. Perdew, K. Burke, and M. Ernzerhof, *Phys. Rev. Lett.* **77**, 3865 (1996).

⁴⁵P. E. Blöchl, *Phys. Rev. B* **50**, 17953 (1994).

⁴⁶G. Kresse and J. Joubert, *Phys. Rev. B* **59**, 1758 (1999).

⁴⁷C. Kaneta, T. Yamasaki, T. Uchiyama, T. Uda, and K. Terakura, *Microelectron. Eng.* **48**, 117 (1999).

⁴⁸N. Takahashi, T. Yamasaki, and C. Kaneta, *Phys. Status Solidi B* **251**, 2169 (2014).

⁴⁹K. Gaál-Nagy, A. Incze, and G. Onida, *Phys. Rev. B* **79**, 045312 (2009).

⁵⁰P. N. Keating, *Phys. Rev.* **145**, 637 (1966).

⁵¹K. O. Ng and D. Vanderbilt, *Phys. Rev. B* **59**, 10132 (1999).

⁵²Y. Tu and J. Tersoff, *Phys. Rev. Lett.* **84**, 4393 (2000).

⁵³Y. Tu and J. Tersoff, *Phys. Rev. Lett.* **89**, 086102 (2002).

⁵⁴S. Lee, R. J. Bondi, and G. S. Hwang, *J. Appl. Phys.* **109**, 113519 (2011).

⁵⁵S. Lee, R. J. Bondi, and G. S. Hwang, *Phys. Rev. B* **84**, 045202 (2011).

⁵⁶The ARTn code with its interface with VASP is available from the authors as well as directly from the site <http://normandmousseau.com>.